The applicability of physical optics in the millimetre and sub-millimetre spectral region. Part I: the ray tracing with diffraction on facets method

Anthony. J. Baran[a,*], Evelyn Hesse[b] , and Odran Sourdeval[c]

[a]*Met Office, Exeter, UK*
[b]*University of Hertfordshire, Centre for Atmospheric and Instrumentation Research, Hatfield, Hertfordshire AL10 9A, UK*
[c]*Institute of Meteorology, Universit¨at Leipzig, Leipzig, Germany*

1st November 2016

JQSRT revised manuscript

*Correspondence to: Met Office, Cordouan 2, FitzRoy Road, Exeter, Devon EX1 3PB, UK. Tel: +44 1392 886162
E-mail address: anthony.baran@metoffice.gov.uk

ABSTRACT

Future satellite missions, from 2021 onwards, will obtain near-global measurements of cirrus at microwave and sub-millimetre frequencies. To realise the potential of these observations, fast and accurate light scattering methods are required to calculate scattered millimetre and sub-millimetre intensities from complex ice crystals. Here, the applicability of the ray tracing with diffraction on facets method (RTDF) in predicting the bulk scalar optical properties and phase functions of randomly oriented hexagonal ice columns and hexagonal ice aggregates at millimetre frequencies is investigated. The applicability of RTDF is shown to be acceptable down to size parameters of about 18, between the frequencies of 243 and 874 GHz. It is demonstrated that RTDF is generally well within about 10% of T-matrix solutions obtained for the scalar optical properties assuming hexagonal ice columns. Moreover, on replacing electromagnetic scalar optical property solutions obtained for the hexagonal ice aggregate with the RTDF counterparts at size parameter values of about 18 and greater, the bulk scalar optical properties can be calculated to generally well within ±5% of an electromagnetic-based database. The RTDF-derived bulk scalar optical properties result in brightness temperature errors to generally within about ±4 K at 874 GHz. Differing microphysics assumptions can easily exceed such errors. Similar findings are found for the bulk scattering phase functions. This finding is owing to the scattering solutions being dominated by the processes of diffraction and reflection, both being well described by RTDF. The impact of centimetre-sized complex ice crystals on interpreting cirrus polarisation measurements at sub-millimetre frequencies is discussed.

KEYWORDS: Absorption; electromagnetic; aggregates; ice; microwave; physical optics; scattering; sub-millimetre; remote sensing.

1. Introduction

The application of sub-millimetre radiometry to the study of the microphysics of ice clouds has been an active area of research since about the latter part of the 1990s. For example, studies by [1-4] have shown that the sub-millimetre part of the spectrum is very sensitive to the column integrated ice water content (IWC), the ice water path (IWP) and to the size distribution function of ice particles (PSD). This is because atmospheric ice at sub-millimetre frequencies is weakly absorbing, relative to scattering, and so the upwelling radiance emitted from below the ice cloud (i.e., from the surface, the gaseous atmosphere, the water and the mixed phase cloud below the cirrus) is largely scattered rather than absorbed. This means that the scattered radiance received by a radiometer above the ice cloud will be depressed relative to the clear sky radiance (owing to the radiance being scattered out of the line of sight of the instrument as a result of multiple scattering and internal cloud scattering).

However, as frequency increases, so does the water vapour continuum [5]. This increase in the water vapour continuum will depend on the location and/or time of the year and may ultimately limit the sensitivity of the sub-millimetre region to particular properties of the ice cloud microphysics. This is because the brightness temperature depressions caused by an increase in atmospheric water vapour loading may also be large and compete with the brightness temperature depressions caused by the ice cloud in certain situations, such as semi-transparent cirrus occurring lower in the atmosphere. However, to account for this water vapour loading effect on brightness temperature depressions, it is usual to retrieve the water vapour loading from the microwave region, but this too requires an accurate understanding of the water vapour continuum, not only throughout the microwave region, but also throughout the sub-millimetre region. Unfortunately, the current understanding of the water vapour continuum in both the microwave and sub-millimetre regions is poor [6], as brightness temperature differences between water vapour continuum models can be as large as 5 K across the microwave and sub-millimetre spectrum [7].

As previously discussed, atmospheric ice at sub-millimetre frequencies is weakly absorbing, and therefore the observed brightness temperature depressions are weakly dependent on the temperature of the atmosphere but are instead more directly related to the IWP [1]. This direct dependence of brightness temperature depression on ice cloud microphysics is a distinct advantage of the sub-millimetre region over the infrared and microwave regions of the spectrum. As the IWP is not directly related to the measured radiance in those two spectral regions, the interpretation of the measurement strongly depends on prior assumptions about the size, orientation, shape and mass of the ice crystals. In the case of the infrared region, the measurement is also dependent upon the temperature of the atmosphere, and in the case of radar reflectivity, its interpretation depends on assumptions about the mass and size of ice crystals. In the latter case, both the mass and size of ice crystals can be simply related to radar reflectivity through the Rayleigh–Gans approximation [8-10]. However, measurements from across the spectrum should be seen as complimentary. For instance, the solar and infrared region will be sensitive to IWP values down to just about 0.5 and up to about 1000 g m^{-2} [11]. Radar reflectivity will be sensitive to the middle and upper range of solar and infrared IWP sensitivity, but it will also significantly exceed the upper range in solar and infrared sensitivity by a number of factors. The sub-millimetre region will be sensitive to a continuum of IWP between the radar reflectivity, and solar and infrared sensitivities. Thus, the sub-millimetre region can act as an important constraint on retrievals of ice cloud properties using radar, solar and infrared radiometric measurements. This is why sub-millimetre instrumentation is required on board aircraft, such as the International Sub-millimetre Airborne Radiometer (ISMAR) [12, 13], and in space to measure the total amount of ice mass contained in the Earth's atmosphere. Ultimately, such measurements will help constrain both climate and numerical weather prediction (NWP) models in their prediction of ice mass and characteristic size of the PSD through their assumed ice microphysics properties.

Of course, the interpretation of microwave and sub-millimetre brightness temperature depressions

will still depend on assumptions about the PSD, ice crystal shape, mass and orientation of the hydrometeors, all of which are currently subject to a considerable degree of uncertainty, see for instance, the following review articles by [14], [15], and references contained therein. The main difficulty in interpreting millimetre and sub-millimetre radiometry is relating the measured brightness temperature depression to an assumed crystal geometry that is consistent with observed mass– and density–size relationships. This further requires representative PSDs that are valid in the mid-latitudes and tropics. In the microwave region, various microphysics assumptions can lead to very large differences in the simulated cirrus brightness temperatures. For instance, in Ref. [16] it is shown that at frequencies centred on 183 GHz, and by assuming a number of PSD parameterizations and density−size relationships, these various assumptions can lead to simulated upwelling brightness temperature differences at top-of-the-atmosphere (TOA) greater than 12 K and 30 K, respectively. Moreover, more recent work by Ref. [17] has shown that different PSDs assumptions to represent the centre microphysics of Hurricane Irene, can also lead to brightness temperature differences between model and observations on the order of about 50 and 70 K at about 183 GHz at TOA. In the sub-millimetre region, Ref. [18] shows that on assuming realistic microphysical variability to generate a variety of cloud states constrained by radar measures of IWC, simulated brightness temperature differences of about 40 and 70 K between about 334 and 874 GHz, respectively, can be realised between the differing cloud states. This range in brightness temperature difference in the sub-millimetre region, between the cloud states, also demonstrates the sensitivity of this spectral region to ice microphysics, such as PSDs, ice crystal shape, and density. To facilitate the simulation of cirrus brightness temperatures at millimetre and sub-millimetre frequencies, there are now a couple of publicly available single-scattering databases of ice crystals. See for instance, the databases developed by Refs. [19] and [20]. These databases are based on the discrete dipole approximation (DDA), which was developed by Ref. [21], to calculate the single-scattering properties of their assumed ice crystal models. The application of the DDA method at the

time limited either the range in frequency or the maximum dimension of ice crystals that could be considered in the construction of each of the databases. In the case of Ref. [19], the frequency does not exceed 340 GHz, and in the case of Ref. [20], the maximum dimension of ice crystals does not exceed 2 mm. Aircraft-based cirrus and ice cloud field campaign in-situ measurements have shown that the maximum dimensions of ice crystals can be significantly greater than 2 mm, indeed ice crystal aggregates can grow to maximum dimensions of several centimetres, see for instance Refs. [22-24]. However, the databases described above do consider a variety of ice crystal shapes, such as solid and hollow hexagonal ice columns, three-dimensional bullet-rosettes, sector snowflake models and hexagonal ice aggregates, among others. Moreover, Ref. [19] considers four temperatures, between 0°C and -40°C, whereas Ref. [20] considers a single temperature of -30°C. Recently, Ref. [25] has demonstrated that absorption by atmospheric ice at sub-millimetre frequencies has a strong dependence on temperature. A further source of uncertainty in the calculation of the single-scattering properties of atmospheric ice is their assumed dielectric properties in the microwave and sub-millimetre regions. For instance, Ref. [26] notes differences in the absorption properties of ice crystals having the same mass of ice between Refs. [19] and [20], which was found to be due to different complex refractive indices being used to construct the two single-scattering databases. Moreover, Ref. [26] recommends the complex refractive indices of atmospheric ice compiled by Ref. [27] to calculate the single-scattering properties of ice crystals at millimetre and sub-millimetre frequencies.

A more recent single-scattering database of atmospheric ice has been made available by [28]. In that paper, sixteen ice crystal models are considered, ranging from single solid and hollow hexagonal ice columns, solid hexagonal plates, solid and hollow bullet-rosettes, hexagonal ice aggregates consisting of column and plate aggregations, among other ice crystal models. The maximum dimensions of each of the ice crystal models range between 2 and 10000 μm, in 24 bins, where the latter sizes are more resolved. The assumed microphysical properties of the ice crystal models that

comprise the database are described in Ref. [29]. The single-scattering properties of the various randomly oriented ice crystal models have been calculated at four temperatures, ranging between -113 and -3ºC, and between the frequencies of 1 and 874 GHz, assuming the complex refractive indices for ice compiled by Ref. [30]. The single-scattering calculations are based on the invariant imbedding T-matrix method of Ref. [31], at most size parameters in the database. At a few of the larger size parameters, the improved geometric optics method of Ref. [32] is applied at the higher frequencies in the database. At these particular size parameters, the so-called "edge effects" are applied to the efficiency factors and to the single-scattering albedo to account for the above-edge and grazing incidence of rays, occurring either above the particle or at its edge, respectively [29, 33, and 34]. These effects must be parameterized into the physical optics method as it does not ordinarily take account of them. To date, this database is the most complete and state-of-the-art, as far as the application of electromagnetic methods is concerned applied to the problem of ice crystal scattering at sub-millimetre frequencies, and so it should find wide application in the interpretation of millimetre and sub-millimetre observations.

However, the previously described databases either suffer from limitations in terms of the frequency of coverage [19] or the maximum dimensions of ice crystals that can be solved for in a timely fashion [20], both references [19] and [20] use the DDA method. Moreover, all databases that are largely based on electromagnetic methods will suffer from the ease of re-computing the ice crystal single-scattering properties in the light of new observations of ice crystal aggregates or compilations of more accurately determined ice crystal refractive indices. To overcome these limitations, the applicability of physical optics in the millimetre and sub-millimetre spectral region is explored in this paper. In principle, if physical optics can be applied in these spectral regions, and down to low enough size parameters, then this would ease the burden of re-computing the optical properties of updated ice crystal models in the light of state-of-the-art observations of ice microphysics or new ice refractive indices that might become available at some point in the future.

In this paper, two physical optics methods are applied. These are: (i) the Monte-Carlo ray tracing method developed by Ref. [35], which includes external diffraction only through the assumption of Fraunhofer diffraction applied at the cross-section of the particle shape, and (ii) the Ray Tracing with Diffraction on Facets (RTDF) method developed by Ref. [36], which incorporates both diffraction at the projected cross-section and diffraction at each of the facets into the ray-tracing paths, and thus, this latter physical optics method is expected to be an improvement over (i). The two physical optics methods are used to compute the scalar optical properties (i.e., the extinction cross-section, C_{ext}, the single scattering albedo, ω_0, and the asymmetry parameter, g) and phase functions. These optical properties are only considered in this paper as they are important for intensity-alone calculations, and the scalar optical properties are applied in very fast radiative transfer models used in numerical weather prediction models to simulate brightness temperature measurements in the microwave [16].

The paper is split into the following sections. Firstly, in Section 2, a brief description of the ISMAR instrument is given, which includes the frequencies considered in this paper. In Section 3, the applicability of the physical optics methods at a number of millimetre (i.e., mm-wave) and sub-millimetre (i.e., sub-mm-wave) frequencies is considered for the cases of randomly oriented hexagonal ice columns and hexagonal ice aggregates. In Section 4, the errors introduced by the RTDF method in computing the upwelling brightness temperatures at a sub-mm-wave frequency are considered. Section 5 discusses implications for ISMAR polarisation observations, under the assumption of randomly oriented ice crystals. Finally, conclusions and discussion are presented in Section 6.

2. The ISMAR instrument

The ISMAR instrument is more fully described by [12, 13], but a brief description is given here. The main objective of ISMAR is to characterise ice clouds in terms of ice crystal size and IWP. The ISMAR instrument is an airborne multi-frequency sub-millimetre radiometer, which should pave

the way towards a space-based instrument so that the main objective can be realised globally

through the Ice Cloud Imager (ICI) instrument, due for launch in 2021. The instrument ISMAR is a

nadir and zenith viewing along-track scanning multi-frequency radiometer, scanning off-nadir

angles between $+55^o$ and -10°, and in zenith, the instrument scans between $+10^o$ and -40°. Table 1

summarises the central locations of the ISMAR frequencies. Table 1 indicates that ISMAR will

resolve spectral information, such as the rotational H_2O and O_2 absorption lines, and the horizontal

and vertical components of polarisation will be measured at certain frequencies. However, this

paper does not discuss the polarisation-induced brightness temperature properties of ice clouds but

does infer such properties from simulations of the degree of linear polarisation of complex ice

crystals, and this is discussed in Section 5 of this paper.

Channels (GHz)	GHz	Polarisation	Feature
243.20	±2.5	Vertical + Horizontal	"Window"
325.15	±1.5, ±3.5, ±9.5	No	H_2O
448.00	±1.4, ±3.0, ±7.2	No	H_2O
664.00	±4.2	Vertical + Horizontal	"Window"
874.40	±6.0	Vertical + Horizontal	"Window"

Table 1: The location of the ISMAR channels, their extent, whether they are polarised, and the atmospheric feature present in each of the channels. The features at each of the channel locations are expressed in terms of whether they are "windows" to emphasise that they can only be considered as partial windows.

As noted previously in the introduction, the water vapour continuum increases with frequency in

the sub-millimetre region of the electromagnetic spectrum [5]. Therefore, the "window" channels

listed in Table 1 can only be considered to be partial, relative to the H_2O and O_2 absorption lines.

Since water vapour increases with decreasing altitude, the lower atmosphere is effectively opaque at

the ISMAR frequencies so surface contributions can be largely ignored [37]. Table 1 demonstrates

that ISMAR has a range of frequencies that should prove useful in determining the properties of an ice cloud, if the cloud is located in the upper troposphere.

Here, we concentrate on the ISMAR frequencies located at 243, 325, 448, 664 and 874 GHz. These channel locations are chosen to contrast the differing absorption properties of atmospheric ice at those frequencies. The channel located at 874 GHz will be installed on the instrument and will be deployed on the Facility for Airborne Atmospheric Measurements (FAAM) BAe 146 G-LUXE aircraft during the summer of 2017. In the next section, with the brightness temperature uncertainties discussed in Section 1 borne in mind, we consider whether the application of the RTDF method is a valid approximation to apply to the microwave and sub-millimetre regions of the spectrum.

3. The applicability of physical optics at mm-wave and sub-mm-wave frequencies

In this section, the applicability of the RTDF and the Monte-Carlo ray tracing methods at mm-wave and sub-mm-wave frequencies are tested by comparing their predicted scalar optical properties and phase functions against the T-matrix method of [38], and to the results from the database compiled by [28]. Here, we assume randomly oriented hexagonal ice columns and hexagonal ice aggregates. The hexagonal ice columns are assumed to be randomly oriented and have an aspect ratio, AR, (i.e., the ratio of column length-to-diameter) of AR=1. The randomly oriented hexagonal ice aggregates developed by Ref. [29, 39] are composed of eight monomer hexagonal elements with varying aspect ratios and are arbitrarily attached. The overall aspect ratio of the hexagonal ice aggregate does not vary as a function of its maximum dimension, D_m, and so the effective density of this model (about 125 kg m^{-3}) remains constant as a function of D_m. The effective density is here taken to be the ratio of the volume of the non-spherical particle to the volume of the sphere of the same D_m, multiplied by the solid density of ice, assumed to be 920 kg m^{-3}. The hexagonal ice aggregate is chosen as the main source of comparison as this type of complex particle is more likely to be sampled by mm-wave and sub-mm-wave instruments as aggregates can grow to cm-sized particles

[22-24]. The complex refractive indices of ice used in the comparisons have been taken from Ref. [30] at the cirrus forming temperature of 230 K (i.e., -44°C). At the frequencies considered in this paper, the relative differences of the real refractive indices of ice between [27] and [30] are generally much less than ±0.5%, whilst the relative difference in the imaginary indices between the two compilations is at most about -10% at 874 GHz. However, at the lower frequencies of between 243 and 448 GHz, the relative differences in the imaginary indices are significantly less than 1%, and at 664 GHz the relative difference is -5%. Given the range of uncertainty in the brightness temperatures, given changing cirrus microphysics assumptions, and variability described in Section 1, these differences are not considered significant for the purposes of the various comparisons presented in this paper.

The relative differences found for the scalar optical properties are plotted as functions of the size parameter, where the size parameter, X, is defined as $\pi D_m/\lambda$, where λ is the incident wavelength. The D_m value found for each of the hexagonal ice columns of AR=1 is the length of the diagonal between the two basal faces of the hexagonal ice column (i.e., $D_m = \sqrt{(D^2+L^2)}$), and the D_m value found for each of the hexagonal ice aggregates has been previously defined in [20]. The relative percent differences, $\varepsilon(v)$, obtained between the T-matrix and the database of [28], and the two physical optics methods are defined as:

$$\varepsilon(v) = \frac{true_v - approx_v}{true_v} \times 100\% \qquad (1)$$

Where in Eq. (1) $true_v$ is taken to be the T-matrix or the database scalar optical property or phase function solutions and the $approx_v$ are the same solutions using the two methods of physical optics. In the sub-section below the results of comparisons between the two physical optics methods and the T-matrix method are presented for the hexagonal ice column.

3.1 The hexagonal ice column

Firstly, comparisons are presented between the two physical optics methods and T-matrix at the frequency of 243 GHz, as this is the lowest frequency and so will have the lowest range in size parameter space that can be used to test the two approximations. The results of the comparisons for all three of the scalar optical properties are presented in Fig. 1a–1c. In Fig. 1(a), results found for the C_{ext} coefficient are plotted as $\log10(C_{ext})$, as this allows differences between solutions found using the T-matrix and physical optics methods to be more discernible. The results of the comparisons shown in Fig. 1a–1c demonstrate that the RTDF method is generally applicable to the calculation of C_{ext} and ω_0 down to X ~ 18, and the prediction of g by RTDF is slightly over-predicted at X~18. The $\varepsilon(\nu)$ error values at X~18 for C_{ext}, ω_0 and g are about 4, < 1, and -8%, respectively. On the other hand, the errors in RTDF at 874 GHz at X~18, found for the same properties, are about 4, -5, and -5%, respectively, as listed in Table 3, where the absolute values are listed in Table 2. The errors in RTDF at the other frequencies are similar to the errors presented here but are not shown for reasons of brevity. The relative percent errors in RTDF are generally less than about 10% at X~18 for all the scalar optical properties considered. Given the uncertainty in the microphysics discussed in Section 1, and the uncertainty in determining, using in-situ measurements, the first order radiative transfer term C_{ext} is of order ±50% [40], errors of less than 10% are acceptable for the application of physical optics to calculate the scalar optical properties at values of X ≥ 18, at least for the hexagonal ice column.

 For intensity-only calculations (i.e., the P_{11} element of the scattering phase matrix is considered alone in radiative transfer calculations), the accuracy of RTDF and Monte-Carlo ray tracing in calculating the P_{11} element at X = 18 needs also to be considered. The results of these comparisons are shown in Fig. 2a–2b.
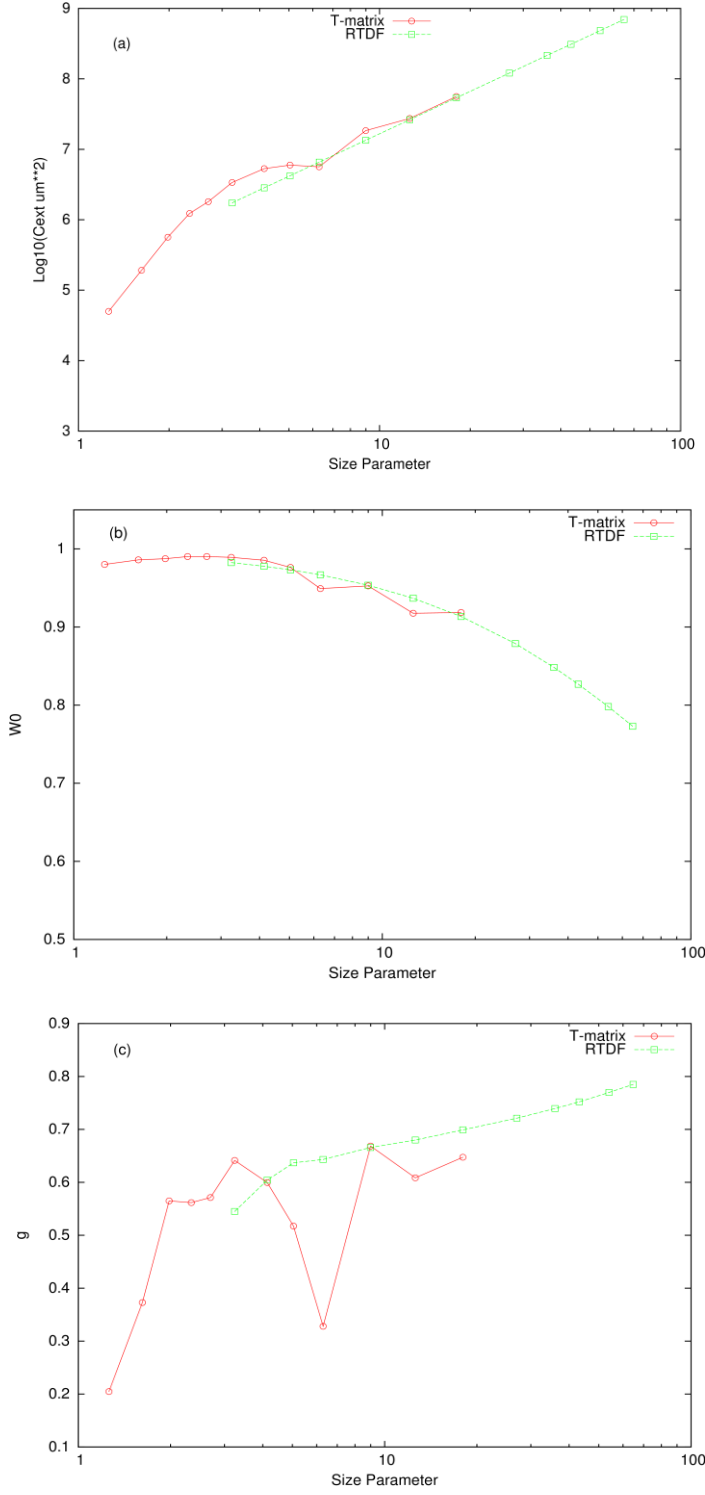
Fig. 1: A comparison between T-matrix (red line) and RTDF (green line) at 243 GHz assuming the hexagonal ice column of AR = 1. Results are shown for (a) $\log_{10}(C_{ext})$, (b) ω_0 and (c) g.

From Fig. 2a–2b it can be seen that the ray tracing method over-predicts the appearance of the halo

at scattering angles $> 62°$. This is not surprising, as ray tracing is known to over-predict halo

phenomena, see for instance Ref. [36]. Moreover, at the scattering angle of 180º, the ray tracing

result completely over-predicts the backscattering peak by nearly one order of magnitude. However, RTDF compares very well against the T-matrix method because of the diffraction of rays entering and leaving the crystal. Note that at 180°, the solution of P_{11} found using the RTDF method is nearly co-incident with the T-matrix result. Diffraction on facets clearly smoothes the halo to very small P_{11} values, which can be seen at the scattering angle of about 70°. The values and relative percent errors found for the scalar optical properties at the frequencies shown in Fig. 2a–2b are listed in Tables 2 and 3, respectively.
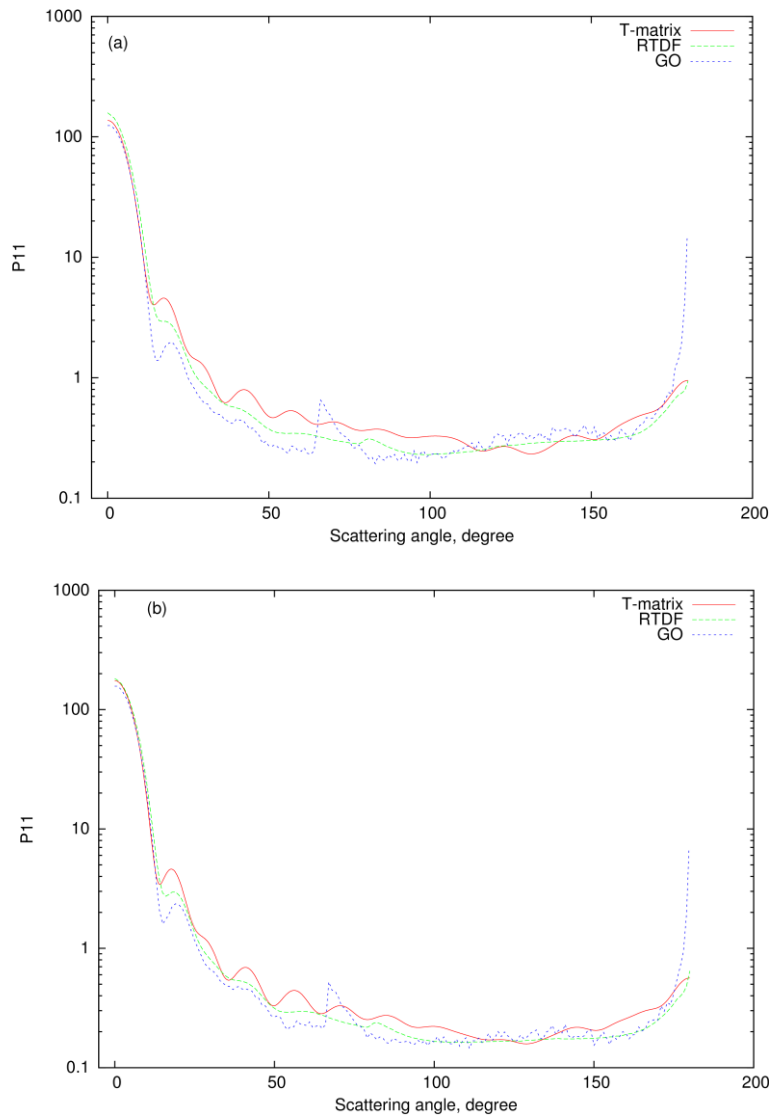

Fig. 2: Comparisons of T-matrix (red line), RTDF (green line), and geometric optics (dashed blue line) solutions found for P_{11} at X~18 as a function of scattering angle, at (a) 243 GHz, (b) 874 GHz. The key is shown in the top-right corner in each of the figures.

The results shown in Table 3 shows that at X ~ 18, the relative percent error found for the physical

optics method in calculating g is at most about -10% using the ray tracing method at the least

absorbing frequency of 243 GHz, which reduces to about -8% when applying the RTDF method. At

the more absorbing frequency of 874 GHz, the relative percent error in g is found to be at most

about -8% using the ray tracing method, which reduces to about -5% when using RTDF. These

relative percent error differences found for g using the two physical optics methods reflect the

variations found in each of the phase functions shown in Fig. 2a–2b. This variation in the phase

functions using the two physical optics methods is reflected in their solutions found for g shown in

Table 2, where the g parameter calculated using the ray tracing method is seen to be over-predicted

relative to the T-matrix and RTDF solutions. However, the solutions found for ω_0, using the two

physical optics methods, are shown to be very similar to each other, as can be seen in Table 2, and

are both within about 5% of the T-matrix result at 874 GHz, but $\varepsilon(\nu)$ for both methods is well

within 1% at 243 GHz.

ν	C_{tm}	ω_{0tm}	g_{tm}	C_{rtdf}	ω_{0rtdf}	g_{rtdf}	C_{rt}	ω_{0rt}	g_{rt}
243	5.62E7	0.9186	0.6473	5.37E7	0.9135	0.6991	5.37E7	0.9149	0.7173
874	4.41E6	0.7043	0.7539	4.21E6	0.7383	0.7907	4.21E7	0.7389	0.8128

Table 2: The solutions found for the extinction coefficient, C, in units of μm^2, the single-scattering
albedo, ω_0, and the asymmetry parameter, g, using the T-matrix method (tm), the RTDF method
(rtdf), and the Monte-Carlo ray tracing method (rt) at the frequencies (ν) of 243 and 874 GHz at
X=18.

ν	$\varepsilon C_{rtdf}\%$	$\varepsilon\omega_{0rtdf}\%$	$\varepsilon g_{rtdf}\%$	$\varepsilon C_{rt}\%$	$\varepsilon\omega_{0rt}\%$	$\varepsilon g_{rt}\%$
243	4.45	0.555	-8.00	4.45	0.403	-10.81
874	4.54	-4.83	-4.88	4.54	-4.91	-7.81

Table 3: The same definitions as in Table 2 except for the relative percent errors, ε, found in the
solutions for the scalar optical properties using RTDF and the Monte-Carlo ray tracing methods at
X=18.

From the results presented in Fig. 2a–2b, it can be concluded that the RTDF method can be applied

at the ISMAR frequencies generally down to X ~ 18 to calculate the scalar optical properties and

the P_{11} element of the scattering phase matrix, at least for the hexagonal ice column. The physical

reason for this accuracy in the RTDF method is owing to the real refractive index of atmospheric ice being around 1.78 at the frequencies shown in the figure. At this refractive index value, the forward transmission as well as external reflection of the incident ray, both undergoing diffraction at the current facet, become the leading terms in the scattering solutions, and these processes are sufficiently well described by the RTDF method, as shown by the two previous figures. In the next sub-section, the applicability of RTDF in calculating the scalar optical properties and phase functions of hexagonal ice aggregates at mm-wave and sub-mm-wave frequencies is explored to ascertain the generality of the result presented in this sub-section.

3.2 The hexagonal ice aggregate

In this sub-section, results found for $\varepsilon(\nu)$ is considered at all the ISMAR frequencies shown in Table 1, and the RTDF method is compared directly against the database results compiled by Ref. [28] using the hexagonal ice aggregate model. Here, the Monte-Carlo ray tracing method is not used owing to the errors previously found in its predicted phase functions shown in Fig. 2a–2b. Firstly, relative errors found for the scalar optical properties plotted as a function of X are presented in Fig. 3a–3c. In the previous sub-section, the size parameter at X~18 was shown to be the size parameter at which errors in RTDF were generally within 10% of the T-matrix solutions. On examination of Fig. 3a–3c at X~18, it can be seen that in Fig. 3a, the error in the RTDF solution found for C_{ext} is at a minimum for all the five frequencies shown, and the error has a value of less than 10%. However, this error increases to a little over 10% at X~30, owing to the well-known interference pattern in C_{ext}, thereafter; the error consistently decreases with increasing size parameter, as the extinction cross-section tends to the geometric optics result of twice the projected area of the particle [33].

Interestingly, the results found for ω_0, presented in Fig. 3b show that the relative percent errors increase with frequency, that is, as absorption increases with frequency, and that at X~18 the largest error in RTDF at 874 GHz is found to be about -4%. The figure also shows that the error at 874

GHz increases to a maximum value of about -5% at a size parameter just greater than about 20. Furthermore, at the lowest frequency of 243 GHz, the error is less than -1% at X~18, whilst at the highest frequency of 664 GHz that will be on board the ICI instrument, the error in RTDF is about - 2% at X~18. Moreover, at X~20, the error in RTDF does increase to a maximum value at all the frequencies shown, but this error is no greater than about -5%. The results found for the RTDF errors in calculating g are shown in Fig. 3c, and these errors are more significant at X~20 than found for the two other scalar optical properties, being greater than -10% at around that size parameter, where the largest errors in RTDF now appear at the least absorbing frequency of 243 GHz. This is presumably due to the stronger interference effects occurring in g, which will be most pronounced at the least absorbing frequency, and these interference effects will be more damped as ice absorption increases with frequency. Interestingly, at X>40, the errors found for g tend abruptly to near zero values, this is probably the size parameters at which the database switches from the invariant imbedded T-matrix and IGOM methods mentioned in Section 1.

The results shown in Fig. 3a–3b found for the hexagonal ice aggregate are not too different from those found for the hexagonal ice column at size parameter values of about 18. The errors in RTDF found for the asymmetry parameter, are however, more significant at X~18 than previously found. The reason for the discrepancies is not only due to interference effects as already mentioned but could also be due to the calculation of the phase functions using the RTDF method. The results of comparing the phase functions at the frequencies of 243 and 874 GHz are shown in Fig. 4a–4b, respectively. The figure shows that the RTDF method follows the general shape of the hexagonal ice aggregate phase function at X~18 rather well at both frequencies at such a low size parameter. However, diffraction at the facets seems to be slightly under-estimated: The back-scattering peak is too sharp and the halo peak is still visible. The same trend occurs for the stronger forward scattering which results in slightly too low side-scattering. As a consequence, the asymmetry parameter is too low.
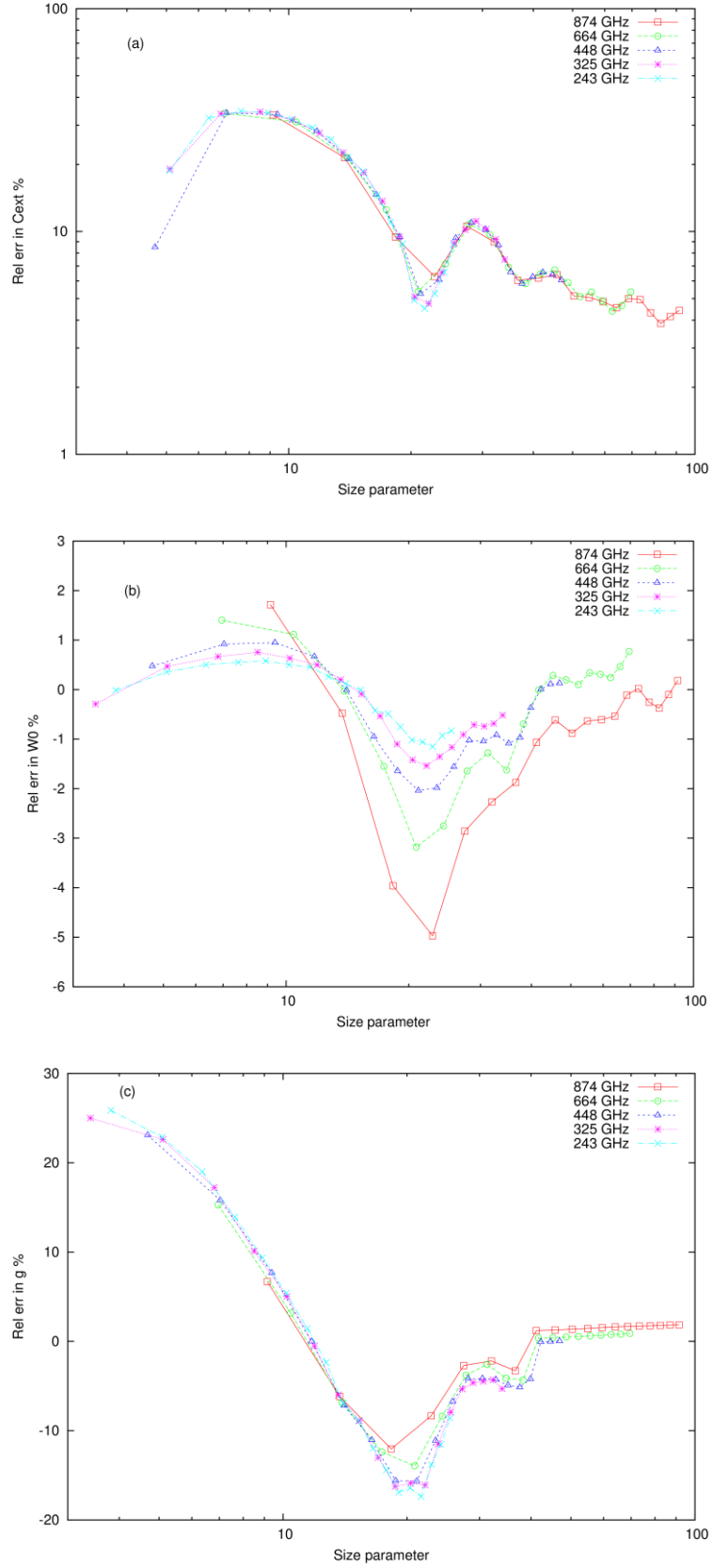
Fig. 3: The relative percent error found for RTDF in calculating the scalar optical properties as a function of size parameter, showing results for (a) C_{ext}, (b) ω_0, and (c) g. The key to each of the frequencies in Table 1 is shown in the top-right corner in each of the figures.

Nonetheless, without the inclusion of diffraction on facets into the physical optics method, then the over-prediction of the halo would become most apparent as in Fig. 2a–2b, and the exact backscatter result would have been more significantly over-predicted if it were not for the smoothing introduced by the inclusion of internal diffraction. Thus, the inclusion of diffraction on facets is critical in the applicability of the physical optics approximation in the mm-wave and sub-mm-wave spectral regions at low size parameters, irrespective of ice particle shape.
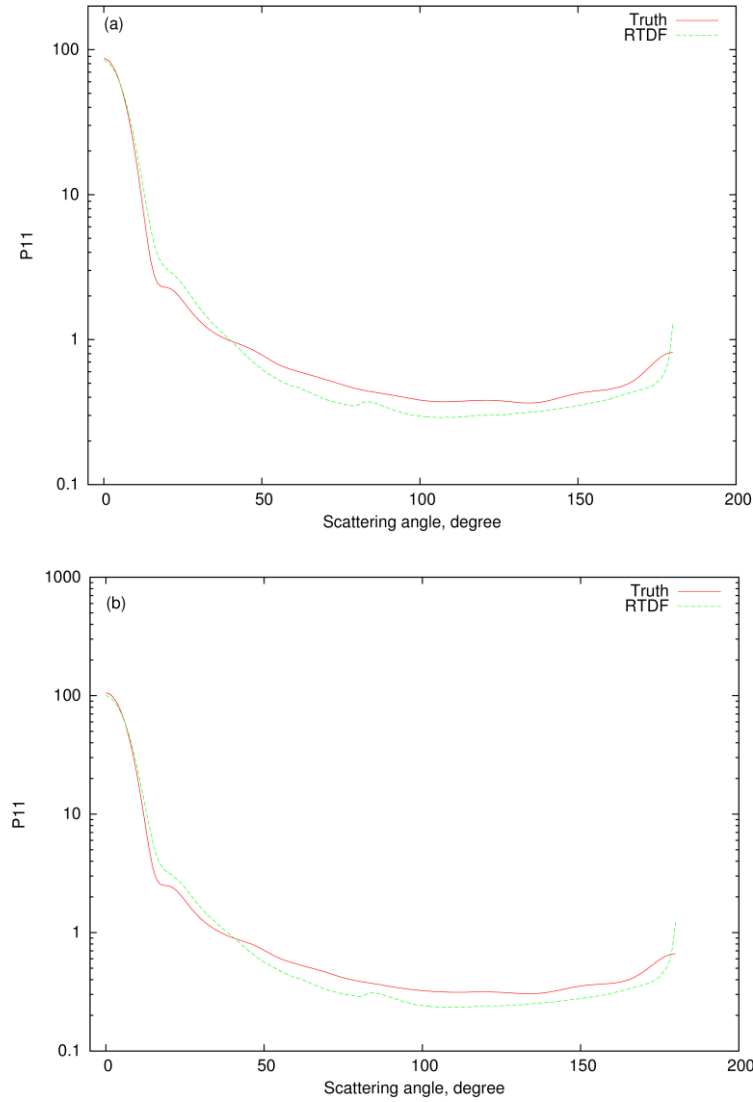

Fig. 4: The predicted phase functions of the hexagonal ice aggregate at X~18 plotted against the scattering angle at the frequencies of (a) 243 GHz and (b) 874 GHz. The true phase functions are from the database [28], which at X~18, applies the invariant imbedding T-matrix method (red line). The RTDF method is shown as the green line. The key is shown in the top-right corner.

A further interesting feature to note in Fig. 4a–4b is that the electromagnetic result is smoother than

the single hexagonal ice column result shown in Fig. 2a–2b. This is probably because the interference effects that occur for the single hexagonal ice column have been smoothed out by the collection of monomer hexagonal ice columns that make up the hexagonal ice aggregate. Conversely, the diffraction intensities on the RTDF calculated phase function have also been smoothed relative to the phase function shown in Fig. 2a–2b for the same reasons. That is, the ice aggregate results in probably an overall averaged result, and this is why the phase functions using both methods appear smoother than their single hexagonal ice column counterparts.

In this sub-section, the RTDF calculated scalar optical properties and phase functions have been compared to the same results from the database at single size parameters. However, in reality, cirrus and ice cloud are composed of a spectrum of ice crystal size characterised by the PSD. In the next sub-section, the accuracy of the RTDF method in calculating the bulk scalar optical properties and bulk phase functions is assessed.

3.3 The effect of PSDs on the accuracy of the RTDF method

In this sub-section, the averaging effects of the PSD on the scalar optical properties and phase functions are explored in relation to the accuracy of the RTDF method at mm-wave and sub-mm-wave frequencies assuming the hexagonal ice aggregate model of Ref. [28]. Here, this is examined using the lowest and highest frequencies given in Table 1, that is 243 and 874 GHz, as this represents the extremes of the frequency range given in that table. The PSDs applied here to the ice optical properties are initially based on a PSD provided by Ref. [41]. The original PSD is artificially changed in number concentration to give a range in characteristic ice particle size, which in this paper is given as the mean mass-weighted size of the PSD. Owing to the mass contained in the PSD being primarily determined by the mass of ice being proportional to the maximum dimension raised to the power of two. The mean mass-weighted size, D_{mmw}, is defined as:

$$D_{mmw} = \frac{\int_{Dmin}^{Dmax} f(D_m) D_m{}^3 dD_m}{\int_{Dmin}^{Dmax} f(D_m) D_m{}^2 dD_m} \qquad (2)$$

where in Eq. (2), D_{min} and D_{max} are the minimum and maximum dimensions contained in the PSD, $f(D_m)$ is the ice crystal number concentration (i.e., in units of m^{-4}) as a function of ice crystal maximum dimension, D_m. The characteristic size D_{mmw} is chosen here as the mass of ice is a prognostic variable in climate and numerical weather prediction models. Therefore, the mm-wave and sub-mm-wave ice optical properties can be related more directly to a model prognostic variable through D_{mmw}. See for instance [42, 43], which discuss the need to relate more directly model prognostic variables in climate and numerical weather prediction models to ice optical properties. Here, $f(D_m)$ has been varied in the constructed PSDs to give a range of D_{mmw} values ranging between 53 and 3324 μm, and the shapes of the 13 PSDs used to give this range in D_{mmw} are shown in Fig. 5. This range in D_{mmw} provides a spectrum of size parameters at the two extreme frequencies on which to base tests of the RTDF method. The PSDs are not taken as actual cirrus or ice cloud PSDs but are used to give a range in size parameter space as mentioned above. However, some of the PSDs do possess a large ice aggregation mode at D_m values greater than about 1000 μm which is observed in real cirrus and iced cloud; see for instance Ref. [44].

Note also the range in D_m shown in Fig. 5 is between 2 and 10000 μm, this exactly matches the maximum dimensions contained in the database of [28]. Furthermore, the smallest value of D_{mmw} is associated with the largest concentration of ice crystals at D_m values less than about 100 μm. Whilst the largest value of D_{mmw} is associated with the PSD having the largest ice aggregation mode at about 3000 μm. This behaviour in D_{mmw} does mimic reality, as the PSDs containing the greatest amount of ice mass will be associated with greater values of mean mass-weighted dimension, and vice versa.
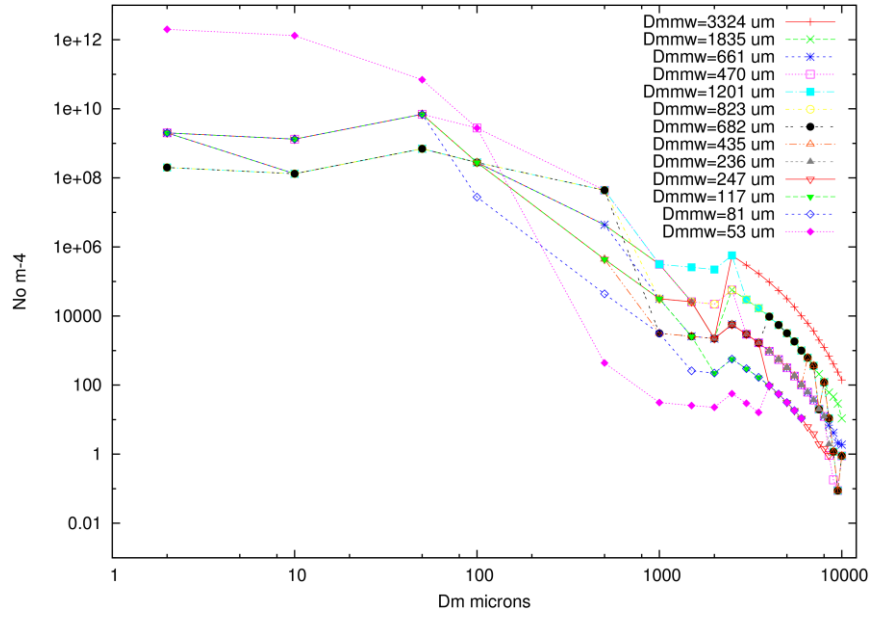
Fig. 5: The ice crystal number concentrations, N_o in units of m^{-4}, as a function of ice crystal maximum dimension, D_m. The key to the PSD shape and the D_{mmw} value for each of the 13 PSDs is shown by the key in the top-right corner in the figure.

These 13 PSDs are applied to calculate the orientation-averaged bulk scalar optical properties. That is, the orientation-averaged bulk extinction and scattering coefficients, $<\beta_{ext}>$ and $<\beta_{sca}>$, respectively, the single-scattering albedo, $<\omega_0>$, the asymmetry parameter, $<g>$, and the phase function, $<P_{11}>$ using the following set of equations:

$$\left\langle\beta_{ext}\right\rangle = \int_{D_{min}}^{D_{max}} f(D_m)\left\langle C_{ext}\right\rangle dD_m \qquad (3)$$

where in Eq. (3), the terms D_{min}, D_{max} and $f(D_m)$ have been previously defined, the term $<C_{ext}>$ is the orientation-averaged extinction cross-section, and $<C_{ext}>$ is of course itself a function of D_m but this dependency has been dropped here and throughout for reasons of clarity.

$$\left\langle\beta_{sca}\right\rangle = \int_{D_{min}}^{D_{max}} f(D_m)\left\langle C_{sca}\right\rangle dD_m \qquad (4)$$

Given $<\beta_{ext}>$ and $<\beta_{sca}>$, $<\omega_0>$ is defined as follows:

$$\langle \omega_0 \rangle = \frac{\langle \beta_{sca} \rangle}{\langle \beta_{ext} \rangle} \quad (5)$$

and the final scalar optical property, <g>, is given by the following equation:

$$\langle g \rangle = \frac{\int_{Dmin}^{Dmax} f(D_m) \langle C_{sca} \rangle \langle g \rangle dD_m}{\int_{Dmin}^{Dmax} f(D_m) \langle C_{sca} \rangle dD_m} \quad (6)$$

Finally, the orientation-averaged bulk single-scattering phase function, $<P_{11}>$ is given by the following equation:

$$\langle P_{11}(\theta) \rangle = \frac{\int_{Dmin}^{Dmax} f(D_m) \langle C_{sca} \rangle \langle P_{11}(\theta, D_m) \rangle dD_m}{\int_{Dmin}^{Dmax} f(D_m) \langle C_{sca} \rangle dD_m} \quad (7)$$

Hereinafter, the <> symbols are dropped from the following discussion for reasons of clarity.

As shown previously in sub-section 3.2, the RTDF model replicated the hexagonal ice aggregate database of scalar optical properties at X values around 18 to within generally ±10%. Here, the database of scalar optical properties and phase functions at X~18, and greater, are interchanged with the corresponding RTDF solutions at those values of X at the frequencies of 243 and 874 GHz and these are then integrated over the 13 PSDs, and compared to the "truth". The truth in this case represents the original database of hexagonal ice aggregate optical properties without interchanging the properties at the two frequencies. The purpose of this procedure is to ascertain the lowest X value at which the ice optical properties can be calculated using RTDF to within an acceptable error, given all the other potential errors discussed in Section 1.

Firstly, the relative percent errors in RTDF for the three scalar bulk optical properties following the above procedure are shown in Fig. 6a–6c at the two frequencies. As expected, the results show that when replacing the database results at X~18, and greater, with RTDF and averaging these over the 13 PSDs, the relative percent errors are significantly reduced at the two frequencies relative to the

results shown in Fig. 3a–3c, this being especially true for g. In that particular case, the relative errors are generally within ±2% for most of the D_{mmw} values shown, which from an application point of view is far more acceptable than previously found for g. Moreover, the errors in the RTDF calculated solutions found for ω_0 are also generally within a few percent and the corresponding errors in β_{ext} are generally well within 10%.

Given that measurement uncertainties in β_{ext} are on the order of ±50% [40], the errors in this parameter shown in Fig. 6a are well within the current experimental uncertainties. The results presented in Fig. 6a–6c show that the errors in RTDF are greater at 874 GHz than at 243 GHz. This result is to be expected, since the interchange of solutions at X~18 is at D_m values of 7000 and 2000 μm at 243 and 874 GHz, respectively. Given that the extent of the PSDs in D_m does not exceed 10000 μm, then it is not very surprising to find that the lower frequency will be least in error when calculating the optical properties using RTDF. Therefore, the RTDF error results shown at 874 GHz presented in Fig. 6a–6c represent the largest possible errors if the more exact results are replaced by RTDF at X~18, and greater. Of course, the errors in RTDF found here will decrease if the exact results are replaced at size parameters greater than about 18. However, it is re-iterated here that the purpose of this sub-section is to find the lowest value of X that is acceptable for practical applications. Since the error in RTDF is greatest at 874 GHz, the comparison of bulk phase functions at 874 GHz is presented in Fig. 7, at the largest D_{mmw} value which gave the greatest relative error found for g shown in Fig. 6c.
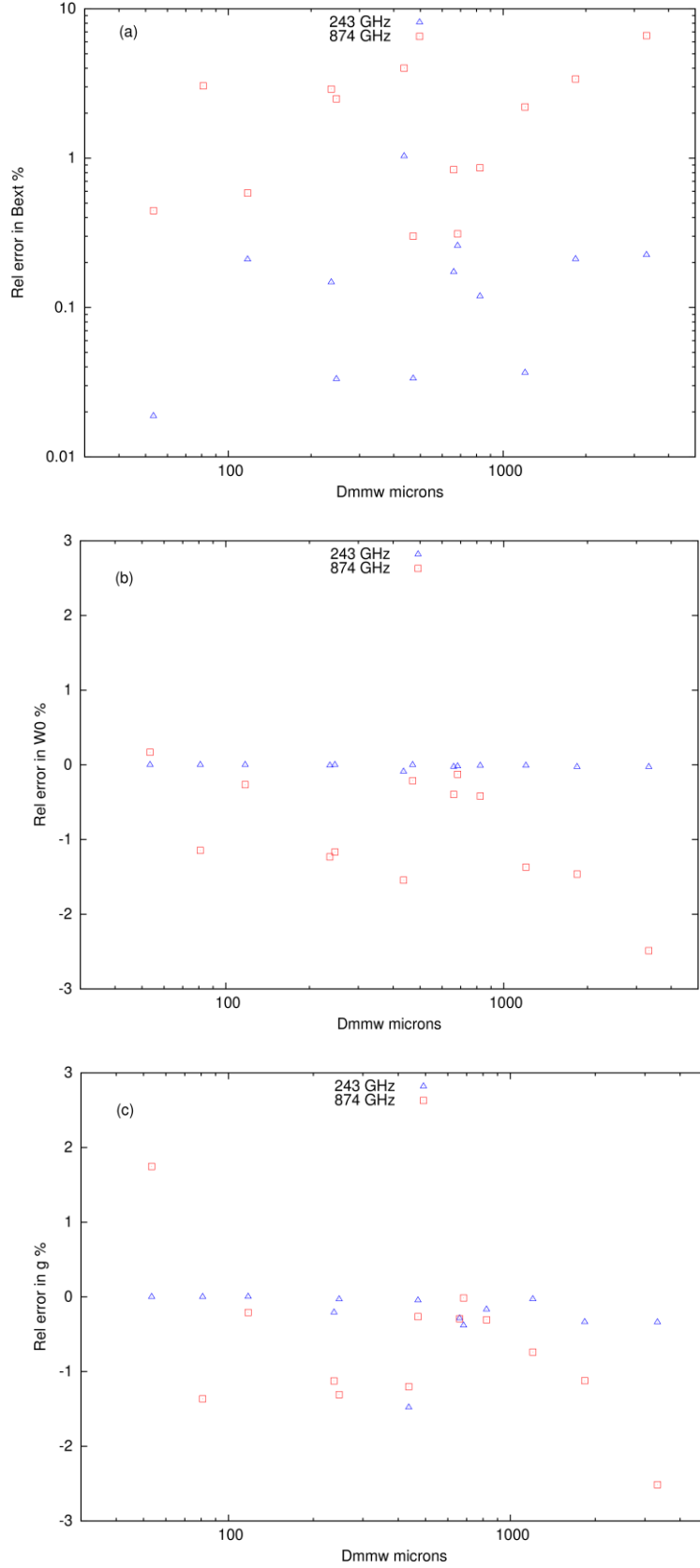
Fig. 6: The relative percent error in the calculated bulk scalar optical properties using the RTDF method at X≥18 plotted against the mean mass-weighted size, D_{mmw}, showing results for (a) β_{ext}, (b) ω_0, and (c) g. The key is shown in the top-centre in each of the figures.
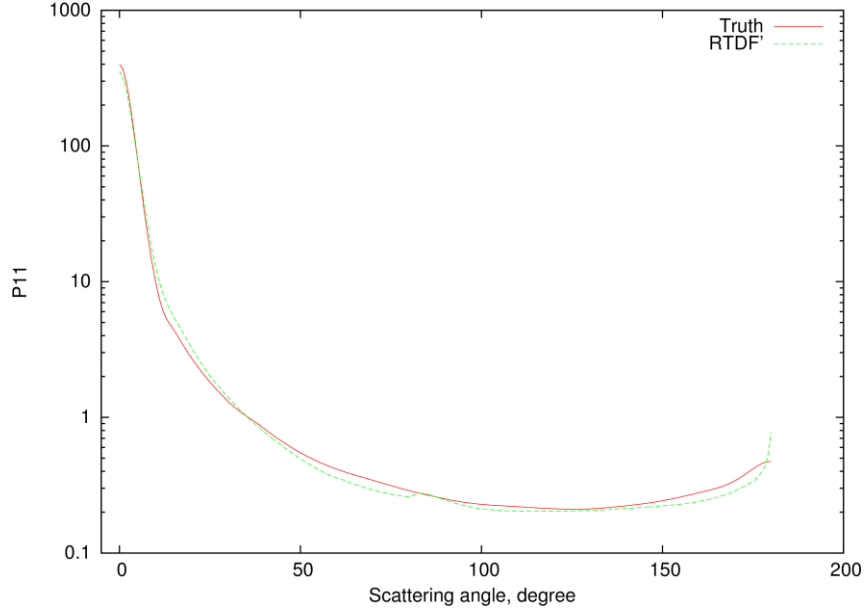
Fig. 7: A comparison of the bulk scattering phase function plotted against the scattering angle between the truth (red line) and RTDF' (green line) calculated at 874 GHz and for D_{mmw}=3324 μm. Where RTDF' means that for X≥18 in the PSD, the phase function solutions are from RTDF.

On comparison of Fig. 7 with Fig. 4b, it can be seen that the bulk calculated phase function is closer to truth than for the RTDF phase function calculated at one single size, especially at the side-scattering angles between about 50° and 150°. In general, the RTDF' solution follows the shape of the phase function, shown in the figure as the truth, generally very well, with still some over-estimation of the backscatter at 180°. It should be borne in mind here that in the sub-millimetre region of the spectrum, the effects of multiple scattering will average out differences between the two phase functions, and most of the radiances measured from above the cirrus or ice cloud will be predominantly emission-based, which means that the forward scattering part of the phase function will become the more important to model correctly. In this respect, the relative percent errors in the RTDF'-based solutions are generally less than about 20% between the scattering angles of 0° and 50°. This sub-section has shown that on replacing more exact solutions with RTDF solutions at X≥18, the bulk scalar optical properties and phase functions can be calculated to within an acceptable range of error that should be of practical value in simulating from above the cloud ISMAR and ICI radiances. That is, given the uncertainties in radiances discussed in Section 1, and

in this sub-section, concerning the measurement uncertainties in determining the bulk extinction coefficient. The meaning of this 'acceptable range of error' is more quantitatively discussed in the next section in terms of the radiative transfer through model cirrus and ice cloud.

4. The brightness temperature errors in applying RTDF at X≥18 in the PSD

In this section, the bulk scalar optical properties derived in Section 3.3 are applied to a radiative transfer model to simulate the ISMAR brightness temperatures at the frequency of 874 GHz. This frequency is selected as the approximation applied in calculating the bulk scalar optical properties introduced in Sub-section 3.3 was in greatest error at that frequency. As a consequence of this, it is necessary to translate the relative errors previously found in the bulk scalar optical properties into errors in brightness temperature space, to ascertain as to whether the errors found in the approximation are of any practical consequences for its application to the interpretation of ISMAR or ICI observations, given the uncertainties in brightness temperatures discussed in Section 1.

The radiative transfer model used here is the delta-Eddington two-stream plane-parallel approximation, and this radiative transfer model has already been described in Refs. [45-47] so a description will not be repeated here. This two-stream approximation is applied as it is the same method used in numerical weather prediction models to simulate brightness temperature measurements in the microwave, see for instance Ref. [16]. The brightness temperatures are found from the simulated radiances using the two-stream approximation by inverting them using the Planck function at the frequency of 874 GHz. In the calculations that follow, the cirrus is assumed to be a single layer and homogeneous, and owing to the anisotropic scattering properties of atmospheric ice (i.e., atmospheric ice has highly peaked phase functions) at the ISMAR frequency, the bulk-averaged scalar optical properties previously described have been truncated using the method of Ref. [48]. This truncation is necessary owing to the strong asymmetric properties of the ice crystal phase function, it is truncated to allow computationally efficient solutions of the radiative transfer equation to be found and to conserve energy, this approximation necessitates re-

scaling the scalar optical properties of the ice crystal. This truncation method in the microwave and sub-millimetre region was previously found to be sufficiently accurate for the purposes of this paper by Ref. [45]. Indeed, Ref. [45] found that in the infrared and sub-millimetre region of the spectrum, the delta-Eddington approximation rarely exceeded root mean square brightness temperature errors of more than a few K assuming nadir viewing geometries. Given the range in uncertainties previously discussed in terms of brightness temperatures, this level of accuracy is considered adequate for the purposes of this paper. In the radiative transfer calculations that follow, the cirrus is assumed to be at an altitude of about 10 km, and above the sea, with no cloud between the sea and the cirrus. The surface and cloud temperatures in all simulations are set to values of 274 and 225 K, respectively. The atmospheric profile assumed in the radiative transfer is the standard mid-latitude winter profile with atmospheric gaseous transmission calculated at the selected ISMAR frequency through the atmospheric layers using MonoRTM (Monochromatic Radiative Transfer Model). The MonoRTM is described in Ref. [49]. The simulations presented here assume a nadir geometry (i.e., directly above the cloud) to minimise the errors in the radiative transfer calculations as previously found by Ref. [45]. Because nadir-only results are shown, linear polarisation at this measurement geometry is identically equal to zero and so in this paper polarised radiative transfer is not currently considered, but will be in later papers.

As previously stated, the bulk scalar optical properties derived in Sub-section 3.3 are applied to the radiative transfer model to simulate the brightness temperatures of model cirrus at 874 GHz. This is achieved by using the bulk-averaged quantities found by using the truth (i.e., the database comprising of the invariant imbedded T-matrix and IGOM solutions), and the method of RTDF being applied at $X \geq 18$ in each of the 13 PSDs, which here is the approximation. The brightness temperature differences are found by subtracting the true from the approximate brightness temperatures, ΔT_b. To derive the brightness temperatures using the two methods, the model cirrus is assumed to have vertical geometrical thicknesses of 1, 3 and 6 km. The results of these simulations

are presented in Fig. 8 at each of the 13 values of D_{mmw}.

The figure shows that at D_{mmw} values less than about 100 μm the ΔT_b values are around zero K, irrespective of cloud depth. This is not too surprising, as at such small D_{mmw} values, the volume extinction coefficient will be very small at 874 GHz and so there will be little attenuation of the upwelling radiation. Therefore, sensitivity will be expected to increase at D_{mmw} values greater than 100 μm, which indeed it does according to the figure. At the smallest cloud depth of 1 km, the ΔT_b values are at their maximum when D_{mmw}=3324 μm, which is about -6 K. However, at such a low cloud depth, as far as the sub-millimetre is concerned, it is unlikely to find such large values of D_{mmw}; the values are more likely to be less than this and so errors of -6 K in the approximation are unlikely to be realised in reality. However, at the larger cloud depths of between 3 and 6 km, at D_{mmw} values greater than about 400 μm, the ΔT_bs are generally within about ±4 K.

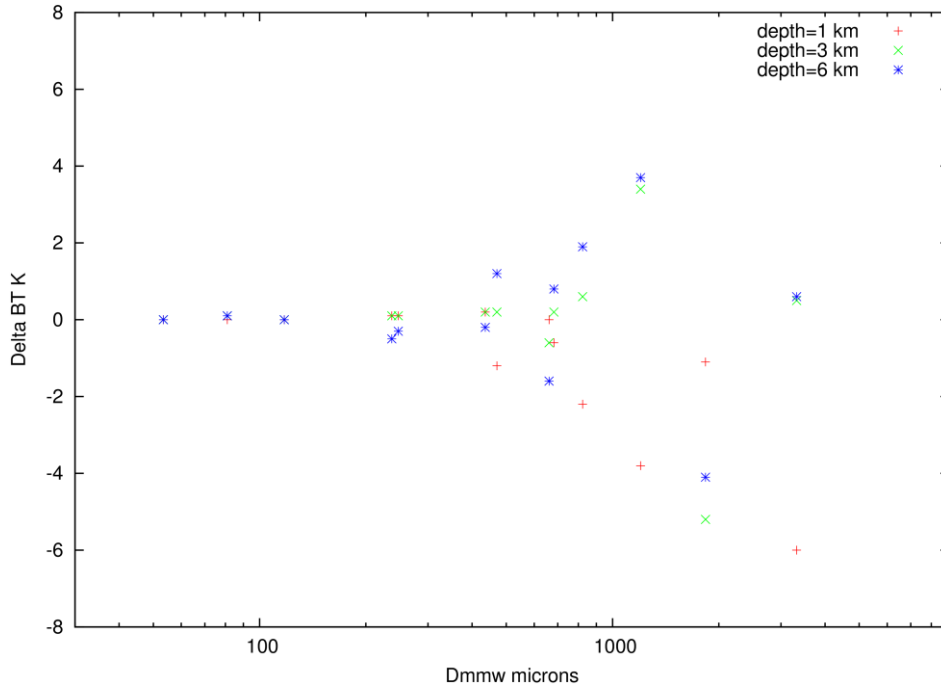

Fig. 8: Brightness temperature differences between the truth and the approximation as a function of D_{mmw}. The simulations are performed assuming cloud vertical depths of 1, 3 and 6 km. The key to the figure is shown in the top-right corner.

At these cloud depths, the attenuation of upwelling radiance is greater due to the increased opacity

of the cloud and so the ΔT_bs will be expected to be smaller than at the cloud depth of 1 km. At the

off-nadir viewing geometries out to 55°, which ISMAR is capable of observing, the errors in the

approximation found here would also be expected to decrease due to the greater slant path

introduced by increasing the sampling angle. Furthermore, at the frequency of 664 GHz, which is

the highest frequency on board the ICI instrument, the errors will be expected to be reduced further

as shown in Sub-section 3.3, owing to as the frequency decreases, the approximation reduces in

relative error. However, a caveat is provided here in that this does depend on the extent of the PSD,

as D_m values of ice crystals can exceed values of 1 cm as noted in Section 1.Putting the errors in the

ΔT_b values found here into context in regard to the uncertainties in brightness temperatures noted in

Section 1, which in the mm-wave spectral regions were on the order of tens of K, the approximation

introduced in this paper appears to be of practical value and should prove useful to apply to the

interpretation of ISMAR and ICI observation in the sub-mm-wave spectral region. It can be

concluded that the RTDF method can be applied at the ISMAR frequencies generally down to X ~

18 to calculate the scalar optical properties and the P_{11} element of the scattering phase matrix.

However, the method is applicable at about this size parameter value owing to the inclusion of

diffraction on facets. This approximation should provide a means to compute the intensities

scattered by complex ice crystals, down to such small size parameters without the need for far more

onerous electromagnetic calculations. The importance of ice crystal complexity, rather than shape

alone, at the ISMAR frequencies is discussed in the next section.

5. The importance of ice crystal complexity at ISMAR frequencies

In this section, the potential impact of ice crystal complexity on the ISMAR polarisation

measurements is studied through the degree of linear polarisation (DLP), which is defined as

P_{12}/P_{11}. This particular polarisation property is chosen as $P_{21}=P_{12}$ under the assumptions of incident

unpolarised light and random orientation, and so P_{12} is related to the Stokes second element Q in

polarised radiative transfer studies, and Q is related to the difference between the vertical and

horizontal components of polarised intensities that ISMAR will measure at certain frequencies

listed in Table 1. The dependence of the DLP on particle size and complexity is studied, in the first

instance, at the frequency of 245 GHz. A frequency at which both ISMAR and ICI will measure

both components of polarised intensities, as this frequency is listed in Table 1 as a "window"

channel. Figure 9a and 9b shows the dependence of the DLP on particle size and on ice crystal

complexity at the frequency of 245 GHz, respectively, assuming the randomly oriented six-

branched bullet rosette, which is discussed and defined in Refs. [35, 50], where the phase matrix

elements have been calculated using the method of RTDF, assuming a temperature of -30 °C. This

temperature is chosen since the size of particles considered is on the order of cm-sized and these

will appear at warmer temperatures in the cloud. The results presented in the figure show that the

measurement of polarisation has a strong dependence on ice crystal size and on ice crystal

complexity. Here the term complexity is used to mean ice crystals that may be made up of many ice

crystal monomers of varying shapes and AR values, which form very complex ice aggregates, and

which might also contain dislocations on their surfaces. This form of complexity is usually referred

to as large-scale complexity; see for instance Ref. [51]. The term "small-scale complexity" is

usually referred to distortions arising from surface roughened ice crystals [51], the scale of which

was recently estimated by Ref. [52] to be on the order of ½ to about one micron, with the height of

roughness having a standard deviation of about 0.1 μm. This estimate of scale roughness was

achieved by using surface roughened sand grains as a proxy for surface roughened ice crystals, as

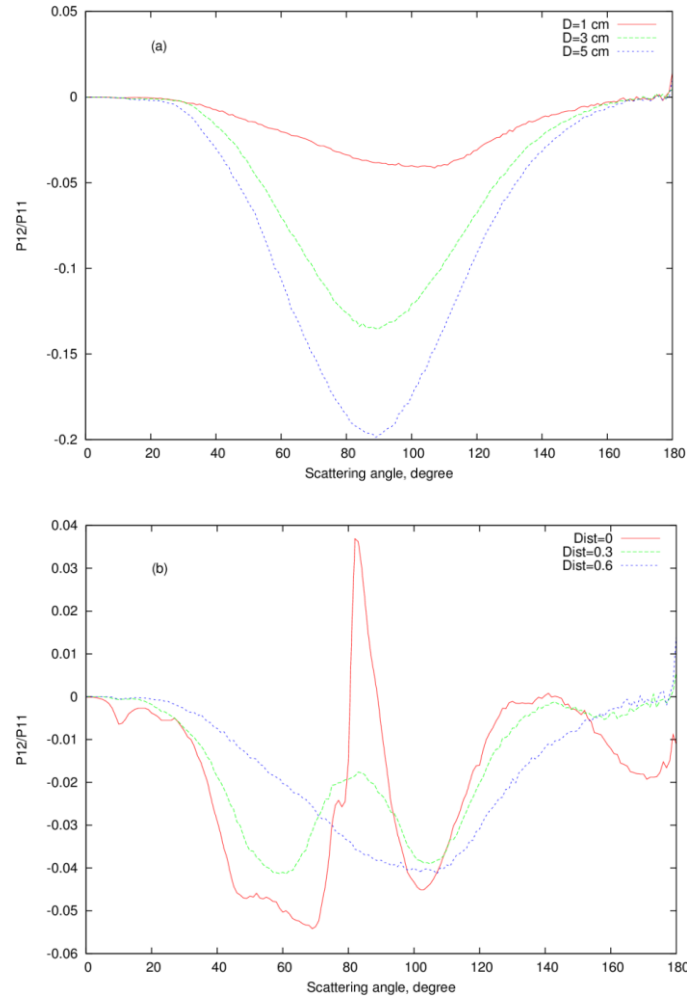the former posses light scattering patterns similar to the latter [53].

Fig. 9: The DLP (P_{12}/P_{11}) plotted against the scattering angle, assuming a randomly oriented six-branched bullet rosette at the frequency of 245 GHz for (a) different sizes of ice crystal assuming a distortion value of 0.6 and (b) different assumed distortion values but for a fixed crystal size of 1 cm. The key in (a) and (b) is shown in the top-right corner.

In this paper, we consider mm-wave and sub-mm-wave scattering, the wavelengths of which are by far much greater than the small-scale complexity that occurs on atmospheric ice. Here, we consider large-scale complexity only. This complexity is represented in the physical optics calculations by re-orienting the surface normal of the facets at each reflection and refraction event, and the degree of complexity is determined by the distortion value, which is defined by Ref. [35]. Distortion values of zero mean "smooth surfaced" particles, and so the scattering phase matrix elements of these particles will retain optical features such as halos and backscattering peaks and troughs. However, distortion values greater than zero will reduce these peaks and halos and, usually, distortion values

of 0.4 or greater will completely remove them, see for instance Refs. [14, 15]. Here, and in the

calculations that follow, we assume distortion values of 0.6 to represent very complex particles that

ISMAR and ICI might sample. Note that in Fig. 9a, the minimum in the DLP does depend on size.

At least for the case of very complex ice crystals, which are the more likely to be sampled.

Moreover, Fig. 9b shows that the sign of the DLP depends on ice crystal complexity and that for

smooth surfaced ice crystals (i.e., distortion value = 0) the sign of DLP can vary between positive

and negative. However, the DLP quickly becomes negative as ice crystal complexity is introduced

through higher distortion values, until finally, at the largest value of distortion assumed here a

single unique minimum in the DLP is observed. Given these findings, it might be possible using

ISMAR-measured polarised brightness temperatures to estimate both the size and complexity of ice

crystals in the form of distortion values. The magnitude of these observed dependencies will depend

on the measurement geometry of the instrument with respect to the cloud, that is, whether or not the

measurements are obtained at angles away from near-forward and near-backscattering as well as on

the PSD and optical depth of the cloud.

In the final part of this section, we consider particle complexity in the form of hexagonal ice

aggregates and explore how potentially important this form of ice crystal complexity is to the

measured ISMAR intensities at the frequency of 880 GHz. Again as shown in Table 1 at this

frequency both the vertical and horizontal components of polarised intensities are measured. To

explore this aspect of ice crystal complexity, we assume randomly oriented hexagonal ice

aggregates in three-dimensional space, which comprise of two-, four- and six-branches. Here, all

aggregates have equal projected areas and have an equal area sphere diameter of 1 cm, and a

distortion value of 0.6 is once again assumed. The dependence of the P_{11} element and the DLP on

ice crystal aggregation at 880 GHz is shown in Fig. 10a and 10b, respectively. The results presented

in Fig. 10a show that as the number of monomers increase from two to six the change in P_{11}, at

such an assumed distortion value, is most noticeable at backscattering angles between about 100°

and 180°, and at forward scattering angles less than about 50°. The increase in the P_{11} element values, as a result of an additional increase in monomers, subsequently lowers the corresponding asymmetry parameter values and increases the single-scattering albedo. This observed decrease and increase in g and ω_0, respectively, is owing to the multiple reflections becoming more important between the individual monomers as the number of monomers is increased. The percentage change in single-scattering albedo and g, in going from the two- to the six-branched hexagonal ice aggregate, is about 4% and 2%, respectively. However, we observe a significant change in the calculated DLP values in going from the two- to the six-branched hexagonal ice aggregate at 880 GHz, and this behaviour is shown in Fig. 10b. From the figure, it is interesting to note that the minimum DLP value is close to that obtained for the very complex six-branched bullet rosette shown in Fig. 9b. Thus, complex particles with high degrees of complexity and which exhibit hexagonal symmetry may have similar polarisation signatures when considering the P_{12} element alone. Further polarised radiative transfer calculations at different frequencies are required to test the generality of this finding. In this section, only centimetre-sized particles have been considered. However, electromagnetic calculations are required at smaller ice crystal sizes to further test the generality of the results presented in this section.

(a)
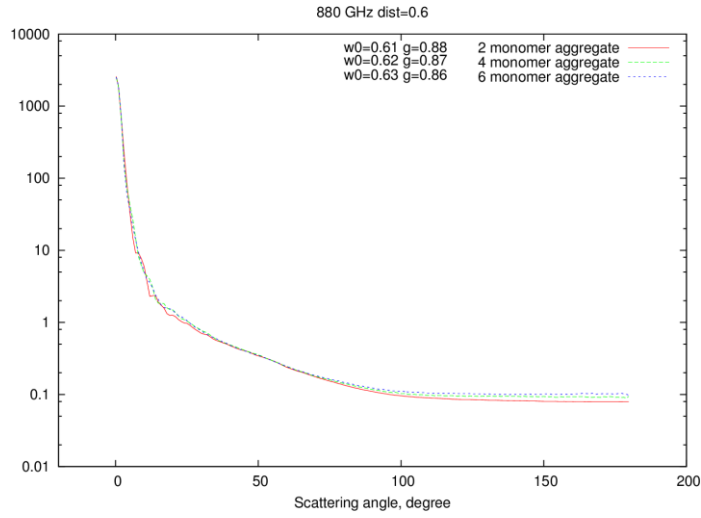
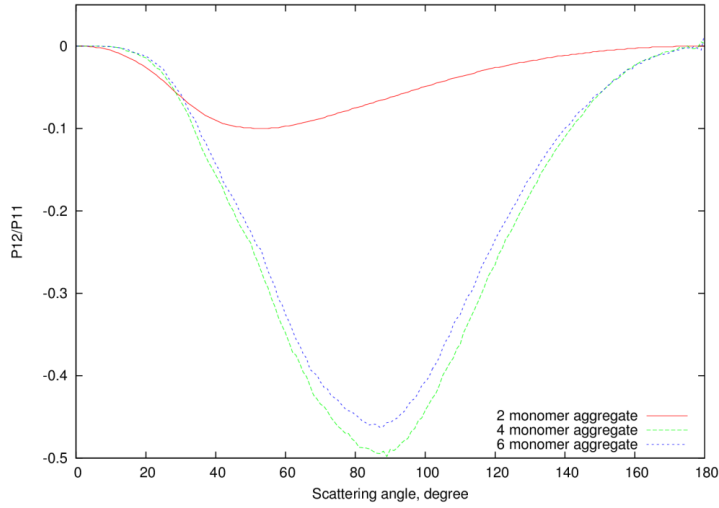

(b)

Fig. 10: The (a) P_{11} element and (b) DLP plotted as a function of scattering angle calculated assuming the randomly oriented two-, four- and six-branched hexagonal ice aggregate. The key in (a) and (b) is shown in the top-right and bottom-right corners, respectively. Also shown in (a) next to the key are results for ω_0 and g calculated for each of the ice aggregate models.

6. Conclusions and discussion

For the first time, this paper has demonstrated that the RTDF method is applicable to the mm-wave and sub-mm-wave frequencies. It has been shown that at selected ISMAR frequencies, between 243 and 874 GHz, the RTDF method successfully replicated T-matrix solutions found for the scalar optical properties, and the scattering phase function, assuming the randomly oriented hexagonal ice column of aspect ratio unity, down to X ~ 18. However, the conventional ray tracing method could not replicate the scattering phase function at the same value of X, owing to the appearance of the halo feature not present in the T-matrix or RTDF solutions obtained for the P_{11} element. Furthermore, at frequencies between 243 and 874 GHz, the RTDF method was also applied to calculate the scalar optical properties and phase functions of the randomly oriented hexagonal ice aggregate, which were compared with the solutions obtained using the invariant imbedding T-matrix and IGOM methods. The RTDF method replicated the more rigorous scalar optical property and phase function solutions at size parameters of about 18, similarly found for the randomly hexagonal ice column, to generally within about 10% for all properties considered at that value of X. The hexagonal ice aggregate was chosen as this model of ice is the more likely type of ice crystal to be sampled by millimetre and sub-millimetre instruments. The physical reason as to why the physical optics methods can be applied at such low values of X at sub-millimetre frequencies is owing to the real refractive index of atmospheric ice at those frequencies being sufficiently large (i.e., ~ 1.78). At such large values of real refractive index, the processes of forward transmission, diffraction and reflection dominate the ray tracing solutions, and these physical processes are well described by the physical optics method.

The RTDF method was also applied to compute the bulk scalar and bulk phase function properties of the hexagonal ice aggregate, and the solutions found were compared to the bulk solutions found from the other two methods mentioned above. Here, at size parameters around 18 and greater, the invariant imbedded T-matrix and IGOM scalar optical property and phase function solutions, called

the rigorous method, were replaced with the corresponding RTDF solutions, called the approximate method. Again, and in general it was found that between D_{mmw} values of about 50 and 3324 µm, the RTDF method replicated the more rigorous solutions to well within 10% for all optical properties considered. Given this finding, the physical optics method can be combined with electromagnetic solutions at X~18 and greater, to compute the bulk scalar optical properties and bulk phase functions of atmospheric ice. This means that publicly available methods such as DDA and T-matrix need only be applied at up to size parameters of around 18 in the mm-wave and sub-mm-wave regions; thereafter, it is important to apply physical optics methods that incorporate internal diffraction, if considering regular smooth surfaced complex particles.

The relative bulk errors found in the RTDF method were also translated into errors found in brightness temperature space at the highest frequency of 874 GHz. At cirrus model depths of 3 and 6 km, the upwelling brightness temperatures, assuming a nadir-pointing geometry, predicted by the approximate method were compared to the brightness temperatures predicted by the rigorous method. The brightness temperature differences found between the two methods were between ± 4 K, at the two assumed geometric depths. Moreover, the larger errors of 4 and -4 K occurred for $D_{mmw} > 1000$ µm. Greater brightness temperature errors in the approximation could be found of up to about -6 K, but these occurred at the cloud geometric depth of 1 km and at the largest D_{mmw} value of 3324 µm. Such large values of D_{mmw} within such geometrically thin clouds are unlikely to occur in reality. However, the range of uncertainty that currently exists in brightness temperatures in the mm-wave and sub-mm-wave parts of the spectrum are on the order of tens of K. These brightness temperature uncertainties arise from uncertainties in PSD, mass– and density–size relationships, the scattering properties of various ice crystal shapes, especially in the sub-millimetre spectral region, and ice crystal orientation. Given the previous uncertainties in brightness temperature and in the cirrus microphysics, the errors found in the approximate method presented in this paper are considered acceptable for practical application to the interpretation of intensity-alone observations

obtained using the ISMAR and/or ICI instruments.

The sensitivity to ice crystal complexity and size, (here centimetre-sized particles were considered which precludes the application of most available electromagnetic methods to this problem), was studied at the frequency of 245 GHz assuming the randomly oriented six-branched bullet rosette. At that frequency, there was a clear dependence of DLP on both size and ice crystal complexity; whereas with the phase function studies, ice crystal complexity was found to minimise differences between the phase functions as complexity increased. Consider here that these polarisation dependencies will also depend on the instrument measurement geometry. Essentially, the further away the measurement is from the forward and the backscattering angles, the dependence of DLP on ice crystal size and complexity increased, because the minimum in DLP often occurred around the scattering angle of about 90°. Further numerical experiments were performed using the hexagonal ice aggregate for understanding the impact of this ice crystal geometry on the DLP at 880 GHz. This was achieved by considering two-, four- and six-branched hexagonal ice aggregates, and as found for the six-branched bullet-rosette, the absolute value in DLP was found to increase as the ice aggregate became more aggregated, and this minimum in DLP was also found to be around the scattering angle of about 90°. For the case of increasingly aggregated and randomised particles, the DLP behaviour was found to be very similar to the randomised six-branch bullet rosette at the same frequency. Therefore, the polarised sub-millimetre region has the potential to be used for the retrieval of ice particle complexity of centimetre-sized objects.

This paper is the first in a series of three. The second paper will consider the application of electromagnetic and physical optics methods to an ensemble model of cirrus particles developed by Ref. [50], which will be used to assess the impact of an ensemble of ice crystals on microwave and sub-millimetre brightness temperature simulations of cirrus. The third paper will be about the application of the developed models to mm-wave and sub-mm-wave observations obtained from a number of cirrus cases.

References

[1] Evans, K. F., S. J. Walter, A. J. Heymsfield, and M. N. Deeter, Modeling of submillimeter passive remote sensing of cirrus clouds, *J. Appl. Meteorol.*, 37(1998), 184– 205.

[2] Wang, J., G. Liu, J. Spinhirne, P. Racette, and W. Hart, Observations and retrievals of cirrus cloud parameters using multichannel millimeter-wave radiometric measurements, *J. Geophys. Res.*, 106(2001), 15,251– 15,263.

[3] Vanek, M. D., et al., Far infrared sensor for cirrus (FIRSC) , An aircraft based FTS to measure the earth radiance spectrum, *Appl. Opt.*, 40(2001), 2169–2176.

[4] Evans, K. F., S. J. Walter, and A. J. Heymsfield, Submillimeter-Wave Cloud Ice Radiometer: Simulations of retrieval algorithm performance, *J. Geophys. Res.*, 107(2002), 10.1029/2001JD0007.

[5] Prigent, C., J. R. Pardo, and W. B. Rossow, Comparisons of the millimeter and submillimeter bands for atmospheric temperature and water vapour soundings for clear and cloudy skies, *J. Appl. Meteor.*, 45(2006), 1622-1633.

[6] Yang, Y., M. Mandehgar, and D. Grischkowsky, Determination of the water vapor continuum absorption by THz-TDS and Molecular Response Theory, *Opt. Express*, 22(2014), 4388-4403.

[7] Turner, D. D., M. P. Cadeddu, U. Lohnert, S. Crewell and A. M. Vogelmann, Modifications to the Water Vapor Continuum in the Microwave Suggested by Ground-Based 150-GHz Observations, *in IEEE Transactions on Geoscience and Remote Sensing*, vol. 47, no. 10, pp. 3326-3337, Oct. doi: 10.1109/TGRS.2009.2022262(2009)

[8] Westbrook, C., R. Ball, and P. Field, Radar scattering by aggregate snowflakes. *Quart. J. Roy. Meteor. Soc.*, 132(2006), 897–914. Corrigendum, 134, 547–548.

[9] Baran, Anthony. J., Bodas-Salcedo, A., Cotton, R. and Lee, C., Simulating the equivalent radar reflectivity of cirrus at 94 GHz using an ensemble model of cirrus ice crystals: a test of the Met Office global numerical weather prediction model. *Q.J.R. Meteorol. Soc.*, 137(2011), 1547–1560, doi: 10.1002/qj.870

[10] Hogan, R. J., and Westbrook, C. D., Equation for the microwave backscatter cross section of aggregate snowflakes using the self-similar Rayleigh–Gans approximation. *J. Atmos. Sci.*,71(2014), 3292–3301, doi:10.1175/JAS-D-13-0347.1

[11] Sourdeval, O., Labonnote, L. C., Baran, A. J., Mülmenstädt, J. and Brogniez, A Methodology for Simultaneous Retrieval of Ice and Liquid Water Cloud Properties. Part II: Near-global Retrievals and Evaluation against A-Train Products. *Q.J.R. Meteorol. Soc*. Accepted Author Manuscript. doi:10.1002/qj.2889(2016).

[12] Baran, A. J., A new application of a multifrequency submillimeter radiometer in determining the microphysical and macrophysical properties of volcanic plumes: A sensitivity study, *J. Geophys. Res.*, 117(2012), D00U18, doi:10.1029/2011JD016781.

[13] Fox, S., Lee, C.., Rule, I., King, R., Rogers, S., Harlow, C. and Baran, A., ISMAR: A new submillimeter airborne radiometer. In *Microwave Radiometry and Remote Sensing of the Environment (MicroRad), 2014 13th Specialist Meeting on* (pp. 128-132). IEEE (2014).

[14] Baran, A. J., From the single-scattering properties of ice crystals to climate prediction: A way forward, *Atmos. Res.*, 112(2012), 45–69.

[15] Yang, P., K. N. Liou, L. Bi, C. Liu, B. Q. Yi, and B. A. Baum, On the radiative properties of ice clouds: Light scattering, remote sensing, and radiation parameterization. *Adv. Atmos. Sci.*, 32(2015), 32–63, doi: 10.1007/s00376-014-0011-z.

[16] Doherty, A. M., Sreerekha, T. R., O'Keeffe, U. M. and English, S. J. (2007), Ice hydrometeor microphysical assumptions in radiative transfer models at AMSU-B frequencies. *Q.J.R. Meteorol. Soc*., 133(2007), 1205–1212, doi:10.1002/qj.84.

[17] Geer, A. J. and Baordo, F., Improved scattering radiative transfer for frozen hydrometeors at microwave frequencies, *Atmos. Meas. Tech*., 7(2014), 1839–1860, doi:10.5194/amt-7-1839-2014.

[18] Rydberg, B., Eriksson, P. and Buehler, S. A., Prediction of cloud ice signatures in submillimetre emission spectra by means of ground-based radar and in situ microphysical data. Q.J.R. Meteorol. Soc., 133(2007), 151–162, doi:10.1002/qj.151.

[19] Liu, G., A Database of Microwave Single-Scattering Properties for Nonspherical Ice Particles. *Bull. Amer. Meteor. Soc*., 89(2008), 1563–1570. doi: http://dx.doi.org/10.1175/2008BAMS2486.1

[20] Hong, G., P. Yang, B.A. Baum, A.J. Heymsfield, F. Weng, Q. Liu, G. Heygster, and S.A. Buehler, Scattering database in the millimeter and submillimeter wave range of 100 - 1000 GHz for nonspherical ice crystals. *Journal of Geophysical Research-Atmospheres*, 114(2009), D06201, DOI: 10.1029/2008JD010451.

[21] Draine, B. T., and P. J. Flatau, Discrete-dipole approximation for scattering calculations, *J. Opt. Soc. Am. A Opt. Image Sci*., 11(1994), 1491–1499.

[22] Field, P. R., A. J. Heymsfield, A. Bansemer, and C. H. Twohy, Determination of the Combined Ventilation Factor and Capacitance for Ice Crystal Aggregates from Airborne Observations in a Tropical Anvil Cloud. *J. Atmos. Sci*., 65(2008), 376–391. doi: http://dx.doi.org/10.1175/2007JAS2391.1

[23] Heymsfield A. J., C. Schmitt C, A. Bansemer, Improved representation of ice-particle masses based on observations in natural clouds. *J. Atmos. Sci*. 67(2010), 3303 – 3318.

[24] Jensen, M., W. Petersen, A. Bansemer, N. Bharadwaj, L. Carey, D. Cecil, S. Collis, A. Del Genio, B. Dolan, J. Gerlach, S. Giangrande, A. Heymsfield, G. Heymsfield, P. Kollias, T. Lang, S. Nesbitt, A. Neumann, M. Poellot, S. Rutledge, M. Schwaller, A. Tokay, C. Williams, D. Wolff, S. Xie, and E. Zipser, The Midlatitude Continental Convective Clouds Experiment (MC3E). Bull. Amer. Meteor. Soc. doi:10.1175/BAMS-D-14-00228.1(2015), in press.

[25] Tang, G., P. Yang, D. L. Wu, Sensitivity study of ice crystal optical properties in the 874 GHz submillimeter band, Journal of Quantitative Spectroscopy and Radiative Transfer, http://dx.doi.org/10.1016/j.jqsrt.2015.12.008 (2016).

[26] Eriksson, P., Jamali, M., Mendrok, J., and Buehler, S. A.: On the microwave optical properties of randomly oriented ice hydrometeors, *Atmos. Meas. Tech*., 8(2015), 1913-1933, doi:10.5194/amt-8-1913-2015.

[27] Mätzler, C., Microwave dielectric properties of ice. Thermal microwave radiation -Applications for remote sensing, *Electro-magn., Waves Ser*., vol. 52, edited by: C. Mätzler, Inst. Eng.Technol., Stevenage, UK, Sect. 5.3, 455–462(2006).

[28] Ding, J., Bi L, Yang P., Kattawar, G. W., Weng F., Liu Q., and Greenwald T., Single-scattering properties of ice particles in the microwave regime: temperature effect on the ice refractive index with implications in remote sensing. Submitted to *J. Quant. Spectrosc. Radiat. Transfer* (2016).

[29] Yang P., Bi L., Baum B. A., Liou K.-N., Kattawar G. W., Mishchenko M. I., and Cole B, Spectrally consistent scattering, absorption, and polarization properties of atmospheric ice crystals at wavelengths from 0.2 µm to 100 µm, *J. Atmos. Sci.*, 70(2013), 330-347.

[30] Iwabuchi H., and Yang P.,Temperature dependence of ice optical constants: Implications for simulating the single-scattering properties of cold ice clouds, *J. Quant. Spectrosc. Radiat. Transfer,* 112(2011), 2520-2525

[31] Bi, L., and P. Yang, Accurate simulation of the optical properties of atmospheric ice crystals with the invariant imbedding T-matrix method. *J. Quant. Spectrosc. Radiat. Transfer*, **138**(2014), 17–35, doi:10.1016/j.jqsrt.2014.01.013.

[32] Yang, P., and K. N. Liou, Geometric-optics-integral-equation method for light scattering by nonspherical ice crystals. *Appl. Opt.*, **35**(1996), 6568–6584, doi:10.1364/AO.35.006568.

[33] van de Hulst., H. C. Light scattering by small particles. New York: Wiley, 1957.

[34] Nussenzveig H. M., and Wiscombe W. J., Efficiency factors in Mie scattering, *Phys. Rev. Lett*.,18(1980), 1490–1494.

[35] Macke, A., Mueller, J., and Raschke, E., Single Scattering Properties of Atmospheric Ice Crystals, *Journal of the Atmospheric Sciences*, 53(1996), 19, 2813-2825.

[36] Hesse, E., Modelling diffraction during ray tracing using the concept of energy flow lines. *J. Quant. Spectrosc. Radiat. Transf.* 109(2008), 1374–1383.

[37] Miao, J., K.-P. Johnsen, S. Buehler, and A. Kokhanovsky, The potential of polarization measurements from space at mm and sub-mm wavelengths for determining cirrus cloud parameters, *Atmos. Chem. Phys*., 3(2003), 39-48.

[38] Havemann S., and A. J. Baran, Extension of T-matrix to scattering of electromagnetic plane waves by non-axisymmetric dielectric particles: application to hexagonal ice cylinders, *JQSRT*, 70(2001),139-158.

[39] Yang, P. and Liou, K. N, Single-scattering properties of complex ice crystals in terrestrial atmosphere, *Contr. Atmos. Phys*., 71(1998), 223–248.

[40] Baran, A.J., Connolly, P.J., Heymsfield, A.J., Bansemer, A., Using in situ estimates of ice water content, volume extinction coefficient, and the total solar optical depth obtained during the tropical ACTIVE campaign to test an ensemble model of cirrus ice crystals. *Q. J. R. Meteorol. Soc*., 137(2011), 199–218.

[41] Fu, Q, An accurate parameterization of the solar radiative properties of cirrus clouds for climate models. *J. Climate*, 9(1996), 2058–2082.

[42] Baran, A. J., Hill P., Furtado K., Field P., and Manners J., A Coupled Cloud Physics–Radiation Parameterization of the Bulk Optical Properties of Cirrus and Its Impact on the Met Office Unified Model Global Atmosphere 5.0 Configuration, *Journal of Climate*, 27(2014), 20, 7725-7752.

[43] Baran, A. J., Hill P., Walters D., Hardiman S.C., Furtado K., Field P. R., and Manners J.,The Impact of Two Coupled Cirrus Microphysics–Radiation Parameterizations on the Temperature and Specific Humidity Biases in the Tropical Tropopause Layer in a Climate Model, *J. Climate*, 29(2016), 5299–5316, doi: 10.1175/JCLI-D-15-0821.1.

[44] Sourdeval, O., E. Gryspeerdt,, J. Delanoë,, P. Kühne,, F. Hemmer, and J. Quaas,, Assessment of the ice crystal number concentration estimated from active space-borne instruments, in preparation for ACP (2016).

[45] Deeter, M. N., and K. F. Evans, A hybrid Eddington-single scattering radiative transfer model for computing radiances from thermally emitting atmospheres, *J. Quant. Spectrosc. Radiat. Transfer*, 60(1998), 635–648.

[46] Rathke, C., and J. Fischer, Retrieval of cloud microphysical properties from thermal infrared observations by a fast iterative radiance fitting method, *J. Atmos. Oceanic Technol*., 17(2000), 1509–1524.

[47] Baran, A. J., The impact of cirrus microphysical and macrophysical properties on upwelling far-infrared spectra, *Q. J. R. Meteorol. Soc*., 133(2007), 1425 –1437.

[48] Joseph, J.H., W.J. Wiscombe and J. A. Weinman, The delta-Eddington approximation for radiative flux transfer. *J. Atmos. Sci.*, 33(1976), 2452-2459.

[49] Clough, S. A., M.W. Shephard, E.J. Mlawer, J.S. Delamere, M.J. Iacono, K. Cady-Pereira, S. Boukabara, P.D. Brown, Atmospheric radiative transfer modeling: a summary of the AER codes, *Journal of Quantitative Spectroscopy and Radiative Transfer*, 91(2005), 233-244, ISSN 0022-4073, http://dx.doi.org/10.1016/j.jqsrt.2004.05.058.

[50] Baran, A. J. and L.-C., Labonnote, A self-consistent scattering model for cirrus. 1: The solar region, *Q. J. Roy. Meteor. Soc.*,133(2007), 1899–1912.

[51] Schnaiter, M., Järvinen, E., Vochezer, P., Abdelmonem, A., Wagner, R., Jourdan, O., Mioche, G., Shcherbakov, V. N., Schmitt, C. G., Tricoli, U., Ulanowski, Z., and Heymsfield, A. J., Cloud chamber experiments on the origin of ice crystal complexity in cirrus clouds, Atmos. Chem. Phys., 16(2016), 5091-5110, doi:10.5194/acp-16-5091-2016.

[52] Collier C. T., Hesse E.,Taylor L., Ulanowski Z., Penttilä A.,Nousiainen T., Effects of surface roughness with two scales on light scattering by hexagonal ice crystals large compared to the wavelength: DDA results, , *J. Quant. Spectrosc. Radiat. Transfer*, 182(2016), 225–239.

[53] Ulanowski Z, Kaye PH, Hirst E, Greenaway RS, Cotton RJ, Hesse E, Collier CT., Incidence of rough and irregular atmospheric ice particles from Small Ice Detector 3 measurements. *Atmos. Chem. Phys.* 14(2014), 1649–62.